Author for correspondence:
Katarina Wolf
e-mail: katarina.wolf@radboudumc.nl

THE ROYAL SOCIETY
PUBLISHING

Cell migration through three-dimensional confining pores: speed accelerations by deformation and recoil of the nucleus

Marina Krause[1,†], Feng Wei Yang[3,†], Mariska te Lindert[1], Philipp Isermann[4], Jan Schepens[1,‡], Ralph J. A. Maas[1], Chandrasekhar Venkataraman[3], Jan Lammerding[4], Anotida Madzvamuse[3], Wiljan Hendriks[1], Joost te Riet[2] and Katarina Wolf[1]

[1]Department of Cell Biology, and [2]Department of Tumor Immunology, Radboud University Medical Center, 6525 GA Nijmegen, The Netherlands
[3]Department of Mathematics, School of Mathematical and Physical Sciences, University of Sussex, Falmer, Brighton BN1 9QH, UK
[4]Meinig School of Biomedical Engineering, Weill Institute for Cell and Molecular Biology, Cornell University, Ithaca, NY 14853, USA

CV, 0000-0003-4039-2056; JL, 0000-0003-4335-8611; AM, 0000-0002-9511-8903;
WH, 0000-0001-9481-8281; KW, 0000-0003-0616-2708

Directional cell migration in dense three-dimensional (3D) environments critically depends upon shape adaptation and is impeded depending on the size and rigidity of the nucleus. Accordingly, the nucleus is primarily understood as a physical obstacle; however, its pro-migratory functions by stepwise deformation and reshaping remain unclear. Using atomic force spectroscopy, time-lapse fluorescence microscopy and shape change analysis tools, we determined the nuclear size, deformability, morphology and shape change of HT1080 fibrosarcoma cells expressing the Fucci cell cycle indicator or being pre-treated with chromatin-decondensating agent TSA. We show oscillating peak accelerations during migration through 3D collagen matrices and microdevices that occur during shape reversion of deformed nuclei (recoil), and increase with confinement. During G1 cell-cycle phase, nucleus stiffness was increased and yielded further increased speed fluctuations together with sustained cell migration rates in confinement when compared to interphase populations or to periods of intrinsic nuclear softening in the S/G2 cell-cycle phase. Likewise, nuclear softening by pharmacological chromatin decondensation or after lamin A/C depletion reduced peak oscillations in confinement. In conclusion, deformation and recoil of the stiff nucleus contributes to saltatory locomotion in dense tissues.

This article is part of a discussion meeting issue 'Forces in cancer: interdisciplinary approaches in tumour mechanobiology'.

1. Introduction

Cell migration is an essential process during development, tissue maintenance and immune function, but is also of importance during pathological cell invasion, including cancer metastasis [1]. Whenever cells (of neoplastic origin) move through connective tissue which consists of spatially and mechanically complex three-dimensional (3D) protein meshworks [2], they respond to mechanical confinement by changing shape. *In vivo*, migrating cells encounter physical challenges composed of microstructural extracellular matrix (ECM) networks and tissue tracks with 1–30 μm width, which are comparable to or smaller than the cell diameter of migrating cells ranging from 8 to 15 μm [3,4]. The nucleus is the largest and stiffest cell organelle that reaches around 2- to

10-fold higher stiffness values than the surrounding cytoplasm [5,6] and plays a pivotal role in cell deformation. Accordingly, under ECM space conditions matching the nuclear diameter, or by cell-derived proteolytic tissue degradation to create a low resistance path that matches the thickest cell diameter, cell migration is not impeded [4]. By contrast, in confining ECM environments, the nucleus will deform and adapt to the constraints of the ECM, but at the same time also form a mechanical obstacle which will gradually slow down migration [4,7–9].

The nucleus is both positioned and transported by the coordinated functions of the leading edge protrusion, integrin attachment to the surrounding substrate, contractile actin cytoskeleton fibres, microtubules and the linker of cytoskeleton and nucleoskeleton (LINC) complex physically linking the chromatin to the cytoskeleton. This leads to alternating force build-up at the front, and contraction of the rear concomitant with rear end integrin de-attachment from ECM, which will move the nucleus forward. Thus, alternating cycles of mechanical pulling and pushing act upon the nucleus during cell migration [4,7,10–12]. Previously, we have proposed a multi-step translocation cycle of the nucleus during confined three-dimensional (3D) cell migration consisting of (I) pressure application by the external constraint onto the nuclear membrane in the direction of migration, (II) beginning deformation of the nucleus by the formation of a local prolapse slowing down migration, (III) gliding of the compressed and deformed nucleus through the pore and (IV) rear release connected to rapid forward pushing and rounding (recoil) of the nucleus [13]. Implicit to this cyclic process, the migration delay during phase II is consistent with the 'physical barrier' function of the nucleus and might represent a phase of storage of deformation energy, which is released as propulsive energy during phase IV, leading to short phases of increased migration. It is, however, not clear whether and to what extent and by which physical characteristics the nucleus contributes to the acceleration of cell migration.

The overall stiffness, or elasticity, of the nucleus in an intact cell is dependent on a number of structural determinants, including A-type lamins that are part of the nuclear lamin network underlying the double nuclear membranes, as well as the organization of chromatin [14–20]. The chromatin packing state is variable and changes according to transcriptional needs, the extent of DNA repair, and the cell cycle phase, particularly when the diploidic G1 stage undergoes DNA replication in S phase to reach the tetraploidic G2-phase stage. Each of these events involves changes in DNA organization, with transient and reversible conversions of dense heterochromatin to more open euchromatin by histone acetylation or de-methylation [21–23]. These two latter processes lead to chromatin decondensation, nuclear softening and concomitant size increase [24–27]. Conversely, chromatin condensation increases nuclear compaction and stiffness in conjunction with a smaller size, as well as migration in wound healing and transwell chamber assays [20]. However, how these complex physical alterations of the nuclear interior impact shape change and migration in 3D confining environments remains to be assessed. In addition, it is unclear how softening of the nucleus, i.e. by lamin A/C reduction [28–30], affects nuclear recoil when cells exit a confined space.

Here, we used independent strategies of altered nuclear elasticity by chromatin condensation state and lamin A/C

expression, and probed how these affect nuclear deformation and reshaping, as well as related migration patterns and rates. By comparing chromatin-compacted G1 cell-cycle phase cells to cells migrating during interphase or S/G2 phase, or by treating cells with the chromatin decondensating compound Trichostatin A (TSA), we co-registered speed oscillations and nuclear deformations. In addition, we developed and adapted a computational approach to calculate fluctuations of nuclear shapes during each migration phase. Our results indicate that deformation of the elastic nucleus during the passage of a constriction generates a recoil event that transforms into nuclear reshaping by rounding and, simultaneously, boosts nuclear propulsion and instantaneous migration velocity.

2. Results

(a) Stiff G1 cell-cycle phase cells maintain fast migration in confinement by shape change

To investigate the effect of the cell cycle on 3D migration, we generated HT1080 cells stably expressing Fucci, a fluorescent ubiquitination-based cell-cycle indicator [31] (electronic supplementary material, figure S1A). The expression of Cdt1-Kusabira-Orange2 in G1 cells and Geminin-Azami-Green1 in S/G2/M cells enabled us to visualize the forward progression of the cell cycle as G1, S-Start and S/G2 phase by detecting either only red, overlapping red and green, or only green signal (figure 1a). From all cells of a subconfluent 2D culture that expressed fluorescence, on average 28% of the cells were in G1, 14% in G1-to-S transition and 58% in S/G2 phase, detected microscopically and generally confirmed by flow cytometry (electronic supplementary material, figure S1B). In accordance with earlier findings [26,31,33], the nuclear area of cells during cycle progression from G1 to S/G2 phase increased by 23% in cell culture or 53% after embedding in 3D collagen matrices, respectively (electronic supplementary material, figure S1C).

To determine the rigidity of the nucleus during cell-cycle progression in HT1080 cells, we probed cultured Fucci sensor-expressing cells by atomic force spectroscopy (AFS), using a bead-coupled cantilever (electronic supplementary material, figure S1D) [34]. With transition from G1 to S/G2 phase, cell deformation increased by 1.4-fold (figure 1b) and, consequently, the calculated elastic moduli in G1 cells (991 ± 415 Pa) decreased by 23% after transit to S/G2 phase (767 ± 455 Pa), in line with previous data using HeLa cells [26]. According to increased chromatin condensation in G1 when compared with S/G2 cells, we calculated a 1.4-fold decrease in dissipation energy in G1-phase cells (electronic supplementary material, figure S1D-G). Collectively, our findings confirmed that cells in G1 have stiffer and less viscous nuclei compared to cells in S/G2, consistent with a higher chromatin compaction status in the G1-phase nucleus.

Next, the impact of cell-cycle progression on HT1080 cell migration efficacy through collagen lattices was tested. During polymerization of collagen into fibrillar networks, interfibrillar spaces of heterogeneous size are formed. Pores that are smaller than the cross-section of the polarized cell body will confine the migrating cell, whereas adjacent, more open spaces will provide sufficient space for forward movement (figure 1c). Consequently, cell and nucleus will
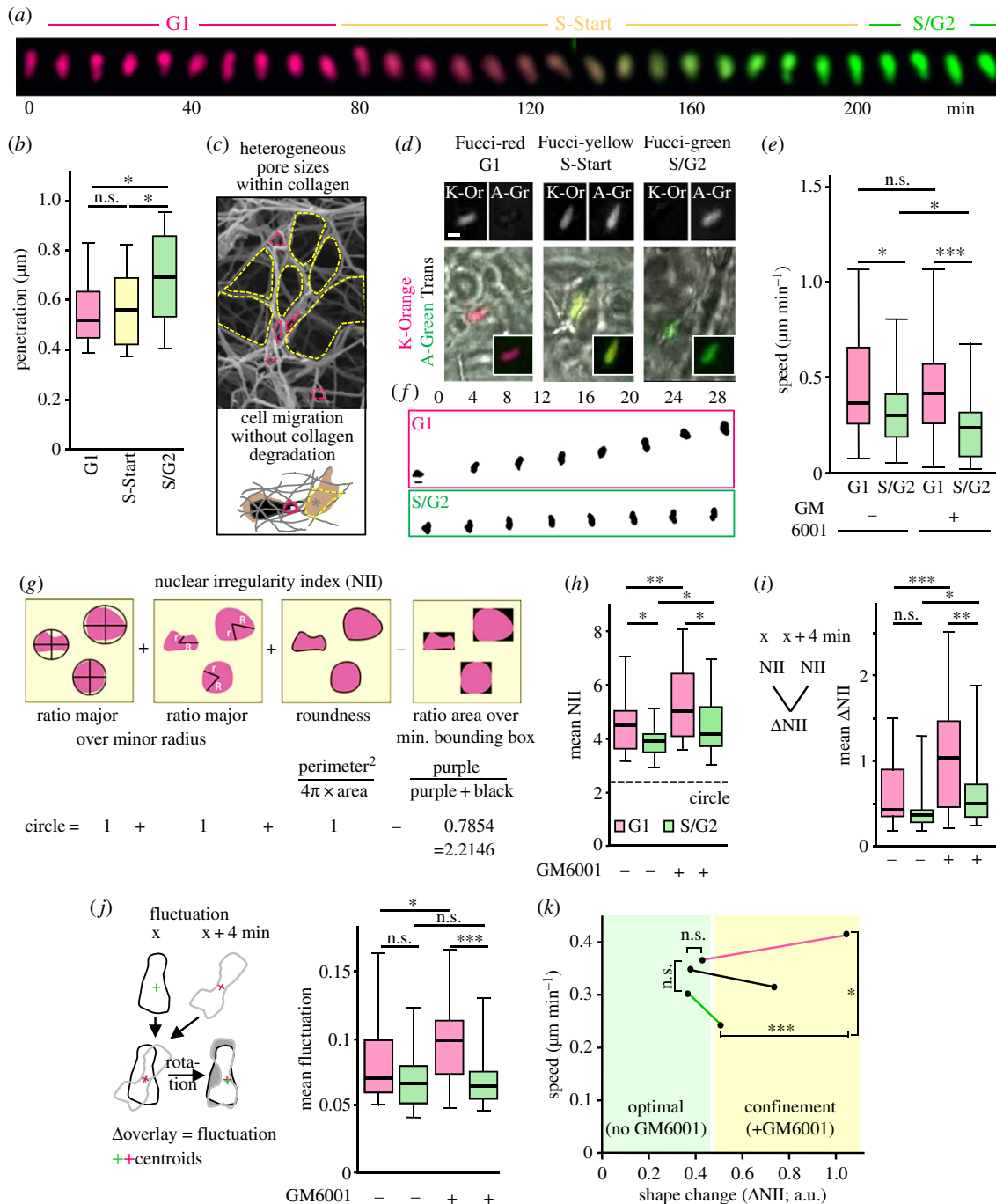
Figure 1. Maintenance of migration through confining pores associates with shape change of the small and rigid G1 cell-cycle phase nucleus. (*a*) Sequence of a cell nucleus from a Fucci-positive HT1080 cell progressing through the cell cycle, as indicated by changing colour coding over 4 h. This sequence is part of electronic supplementary material, figure S2 and Movie S1. (*b*) Quantification of cell deformation (penetration) after 2 nN contact force by a bead-coupled cantilever connected to an atomic force microscope (quantified from the approach curve; electronic supplementary material, figure S1D). $N = 3$; $25 - 32$ cells per indicated cell-cycle phase. (*c*) Top, example of collagen matrix (monitored by scanning electron microscopy as shown in Wolf *et al.* [4]) showing small pore areas (confining; marked in pink), adjacent to large pores (marked in yellow). Bottom, cartoon depicting cell and nucleus in collagen of heterogeneous, colour-coded pore areas, including open space for translocation of cell and nucleus (asterisk). (*d* – *f*) HT1080-Fucci cells migrated in collagen (1.7 mg ml^{-1}) in the presence of matrix metalloproteinase (MMP) inhibitor GM6001 (except where the absence of GM6001 is indicated), as monitored by pathway microscopy. (*d*) Examples of migrating cells at different indicated cell-cycle phases. Image bar, 10 μM. (*e*) Averaged migration speed of single cells from Fucci-red or -green populations from movies of $5 - 24$ h length at indicated conditions. Because the S-start phase covers a short, around 2 h, time period, from here on and in all further experiments G1-phase cells were compared with S/G2 cells only. $N = 2 - 3$; $40 - 65$ cells per condition. (*f*) Nuclear segmentation of migrating HT1080-Fucci cells. Time in minutes as indicated. (*g* – *j*) Nuclear shape analysis. (*g*) Top, schematic illustration of the components used for the calculation of the nuclear irregularity index (NII), adapted from Filippi-Chiela [32]. Bottom, calculation of all components that describe a circle, resulting in a NII of 2.2146. (*h*) Mean NII values per cell were computed and calculated from each nuclear shape sequence over time. (*i*) Left, scheme for calculation of the difference between subsequent NIIs as ΔNII, where rapid shape change of the nucleus results in a high ΔNII value. Right, mean values of ΔNII from each nuclear shape sequence over time. (*j*) Nuclear fluctuation analysis, sketching the analysis procedure (left), and mean values of the fluctuations from each nuclear sequence to the next (right). In (*h*–*j*), mean value per cell over $36 - 316$ min; $n = 3$; $26 - 38$ cells per condition. (*k*) Summary of speed as a function of nuclear shape change (ΔNII) in optimal and confining collagen conditions (data are from (*e*,*i*). Dots connected by red line represent G1 cycle cells; by green line, S/G2 cycle cells; by black line, G1 and S/G2 cycle cells together. (*b*,*e*,*h*,*i*,*j*) Black horizontal lines, boxes and whiskers show the medians, 25th/75th, and 5th/95th percentile (*b*, 10th/90th percentile), and ***, $p \leq 0.001$; **, $p \leq 0.01$; *, $p \leq 0.05$; ns, non-significant (Mann–Whitney test).
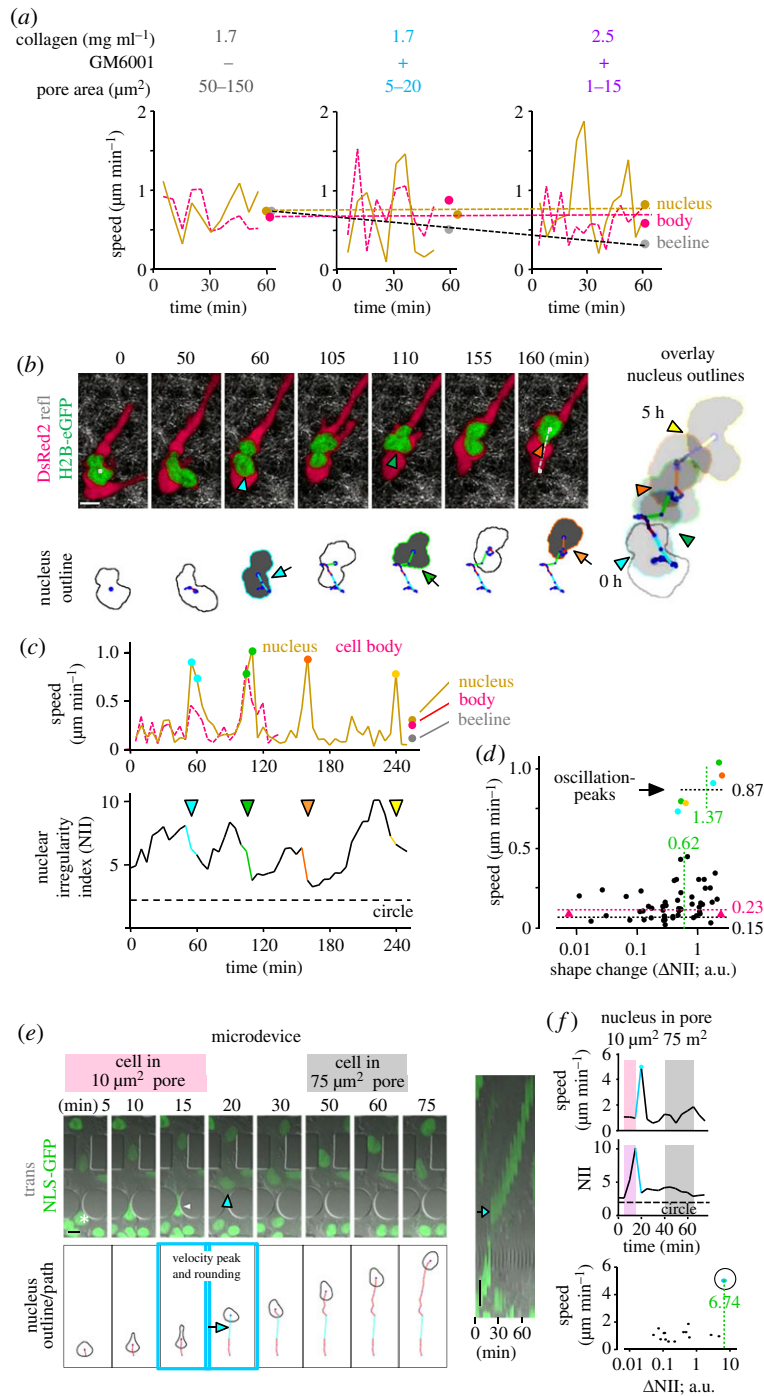
Figure 2. (*Overleaf.*) Speed oscillation and rapid nuclear rounding during cell migration in confining pores. HT1080 fibrosarcoma cells moved either in collagen (*a–d*) or in a synthetic microdevice (*e,f*). (*a*) Cells migrated in collagen of increasing density and the absence or presence of GM6001 as indicated, resulting in depicted decreasing effective pore areas (top; [36]). From each cell, speed of nucleus and cell body was quantified from the migration tracks from the centre of the nucleus as well as the cell body that often demonstrated synchronous speed peaks. Overall migration speed was measured as 'beeline' between the centre of the nucleus from the first and last image as depicted in electronic supplementary material, figure S4 and normalized over 55 min. (*b–d*) Oscillatory speed peaks of both cell and nucleus coincide with nuclear rounding. (*b*) Upper row, left, sequences of HT1080 dual-colour cell moving within high-density bovine collagen (3.3 mg ml^{-1}) monitored by confocal microscopy at 37°C at 5 min intervals [13]. White dots at first and last image and dotted white line indicate position and beeline of the migrated nucleus. Lower row, left, outlines of the nucleus generated from H2B-eGFP signal, with centroids (blue dots) and centroid-connecting movement trajectories in red. Long trajectories indicated in cyan, green and orange and by arrows represent peak movements, and respective nuclear roundings are marked by coloured outline and grey area. Right, overlay of the first and all rounded outlines, and trajectory of the nucleus over 5 h (corresponding to electronic supplementary material, Movie S4). (*c*) Upper graph, step-to-step and average speed quantification from the movement trajectories of moving cell body and nucleus from (*b*), as well as the beeline of the migrated nucleus. Repeated speed peaks (oscillations) of the nucleus are indicated by respective coloured dots. Lower graph, corresponding repeated phases of nuclear rounding measured as NII, indicated by respective colours and arrowheads. (*d*) Speed as a function of ΔNII per time step (=dot) of the moving nucleus shown in (*b*), and quantified in (*c*). All numbers and dotted lines in black and green indicate medians of speed and ΔNII, respectively, for either coloured oscillation peaks or all remaining dots. Dotted line and number in pink indicate speed median from all dots. (*e*) Migration in microdevice of 10 and 75 μm^2 pore areas (corresponding to electronic supplementary material, Movie S5, part 2). Left, upper row, sequence of migrating cell over indicated time. White arrowhead, deformed nucleus in pore. Arrowhead in cyan indicates rounding. Lower row, nuclear outlines with centroids as blue dots and trajectories in red. Arrow indicates long trajectory in cyan that corresponds to nucleus rounding. Right, kymogram visualizing rapid forward movement (arrow) after transmigration of narrow pore. (*f*) Speed and corresponding shape, with colour coding indicating respective pores in (*e*). Bottom, speed–nuclear shape change relationship; number in green, ΔNII value for peak oscillation. Reprinted modified images in (*b*) are with permission from Elsevier [13]. All image bars, 10 μm.

repeatedly deform during migration. In addition, many activated or cancer cell types, including HT1080 fibrosarcoma cells, express a range of matrix metalloproteinases (MMPs) such as MMP-14. These cells migrate through confining collagen matrices by proteolytic remodelling of collagen fibrils, creating paths with $50–100\ \mu m^2$ pore areas that match the respective cell cross-sections [35]. In this setting, MMP broad-spectrum inhibitor GM6001 inhibits collagen degradation and therefore increases the deformation of cell and nucleus during migration through confining collagen of around $5–25\ \mu m^2$ pore size [36]. To test in context how cell deformation and migration speed are altered with transit from G1 to S/G2 phase, migrating HT1080-Fucci cells were optically separated into Fucci-red, -yellow and -green (figure 1d). Proteolytic migration speed of a G1 phase cell population in 3D collagen lattices was $0.4\ \mu m\ min^{-1}$ and reduced by 18% in S/G2-phase cells, whereas at conditions of confinement, migration in S/G2 cells was increasingly compromised by 42%, reaching $0.23\ \mu m\ min^{-1}$ (figure 1e). A similar 50% deceleration in speed, and concomitant area increase, was confirmed during the migration of a single cell during transition from G1 to S/G2 phase (electronic supplementary material, figures S2A-B; C, two most upper graphs; electronic supplementary material, Movie S1). The reduced migration rates of the S/G2 cell population, especially in confinement, may result from complex nuclear properties, including increased nuclear size and chromatin decondensation during S-phase and prior to mitosis, combined with reduced cell adhesion and actomyosin-mediated stiffness [26]. We asked, however, how cells in G1 phase could maintain speed in confinement despite a comparably stiffer nucleus.

To gain insight into the extent of nuclear deformation relative to speed changes during migration in confinement, we thresholded nuclear shapes (figure 1f; electronic supplementary material, Movies S1, right section; S2) and quantified respective shape changes over time as nuclear irregularity index (NII; figure 1g) [32]. The NII determines the level of shape deviation of the nucleus from a circle, and was chosen over more widely used nucleus roundness measurements because of its higher sensitivity (electronic supplementary material, figure S3). Whereas nuclei in moving S/G2-phase cells were more roundish, nuclei in G1 phase adopted somewhat more irregular shapes, which further increased by the presence of GM6001 (figure 1h). The changes between these shapes over consecutive time points were similar during proteolytic migration but, when MMPs were inhibited, increased by 2.4-fold in G1 phase but only 1.3-fold in S/G2 phase cells (figure 1i). To support these findings on dynamic nuclear shape changes, we included nuclear fluctuation analysis (figure 1j, left; electronic supplementary material, Movie S3). This tool calculates the difference between consecutive nuclear shapes, and thus the shape change. To exclude errors owing to a directional change of a cell during migration, nuclear shapes were rotated for maximal overlap. Again, nuclei in G1 phase showed more profound shape fluctuations in the presence of GM6001 whereas S/G2 cell nuclei did not change their shape at all (figure 1j, right). In combination, these two methodologies complement each other for robust measurement of nuclear shape change, and are applicable to all types of shape changes of biological objects over time and location. Together, in contrast to S/G2 phase or mixed G1/S/G2 cell populations, G1-phase cells maintained migration speed in confinement, associated with elastic deformation of the nucleus (figure 1k).

(b) Deformation–rounding cycles of the nucleus correlate with speed oscillations

To approach how deformation of the nucleus may support cell migration, the velocity of cell body, nucleus and the overall migration efficiency were recorded together with the nuclear morphology. To collagen lattices of decreasing pore sizes from around 100 to $10\ \mu m^2$, HT1080 cells responded with a gradual decline of overall migration efficacy ('beeline'; figure 2a), consistent with our previous report [4]. At the same time, the speed of both nucleus and cell body remained unperturbed owing to increasing oscillations (figure 2a), with the nuclear shape increasingly co-fluctuating (electronic supplementary material, figure S4, middle column). These speed and shape fluctuations corresponded to lateral 'swinging' of both nucleus and cell relative to the main axis of movement (figure 2b; electronic supplementary material, Movie S4; figure S4, left column). In parallel, increasing nuclear deformations preceded rapid nuclear rounding (figure 2b, grey filled nuclear outline; c, bottom). At oscillation peaks, nuclear shape change doubled from 0.62 to 1.37 (figure 2d), while the cell body remained elongated. Every nuclear rounding event was precisely accompanied by an up to sixfold accelerated speed peak, each moving the nucleus by about half of its diameter forward (figure 2c, top; b, right). Accelerations versus remaining steps were on average 0.87 versus $0.15\ \mu m\ min^{-1}$, increasing overall migration of the nucleus by 50% ($0.23\ \mu m\ min^{-1}$; figure 2d), as well as similarly the cell body. To support these findings in a migration model that enabled the visualization of the nucleus through pores of defined shape and size, a polydimethylsiloxane (PDMS)-based microdevice was used [37]. As in 3D collagen, migration through $10\ \mu m^2$ pores was followed by nuclear rounding and concomitant speed acceleration, whereas movement through $75\ \mu m^2$ pores lacked both nuclear shape change and speed oscillation (figure 2e,f; electronic supplementary material, Movie S5). Acceleration was several times higher as in collagen and possibly, owing to the higher elastic energy stored in the $5\ \mu m^2$ small nuclear deformation, the result of a higher propulsive energy release into the barrier-free spacing following the tight pore. Taken together, cell passage through extracellular porous confinement coincides with nuclear deformation and is followed by piston-like acceleration of the nucleus together with transient rounding.

(c) Saltatory propulsion of the rounding cell nucleus during migration in confinement is increased in G1-phase cells

Sustained migration in confined 3D environments in G1 cell-cycle phase (figure 1k) is in line with a proposed promoting effect of chromatin condensation on cell migration [20,38], yet the mechanism of speed gain remains unclear. The above-described data suggest that the nucleus acts as obstacle during cell passage through small pores during phase II, but in addition supports migration in phase IV by pushing through the confinement and regaining roundish shape (figure 3a). To further characterize this last step of the transmigration process, we mapped nuclear speed and
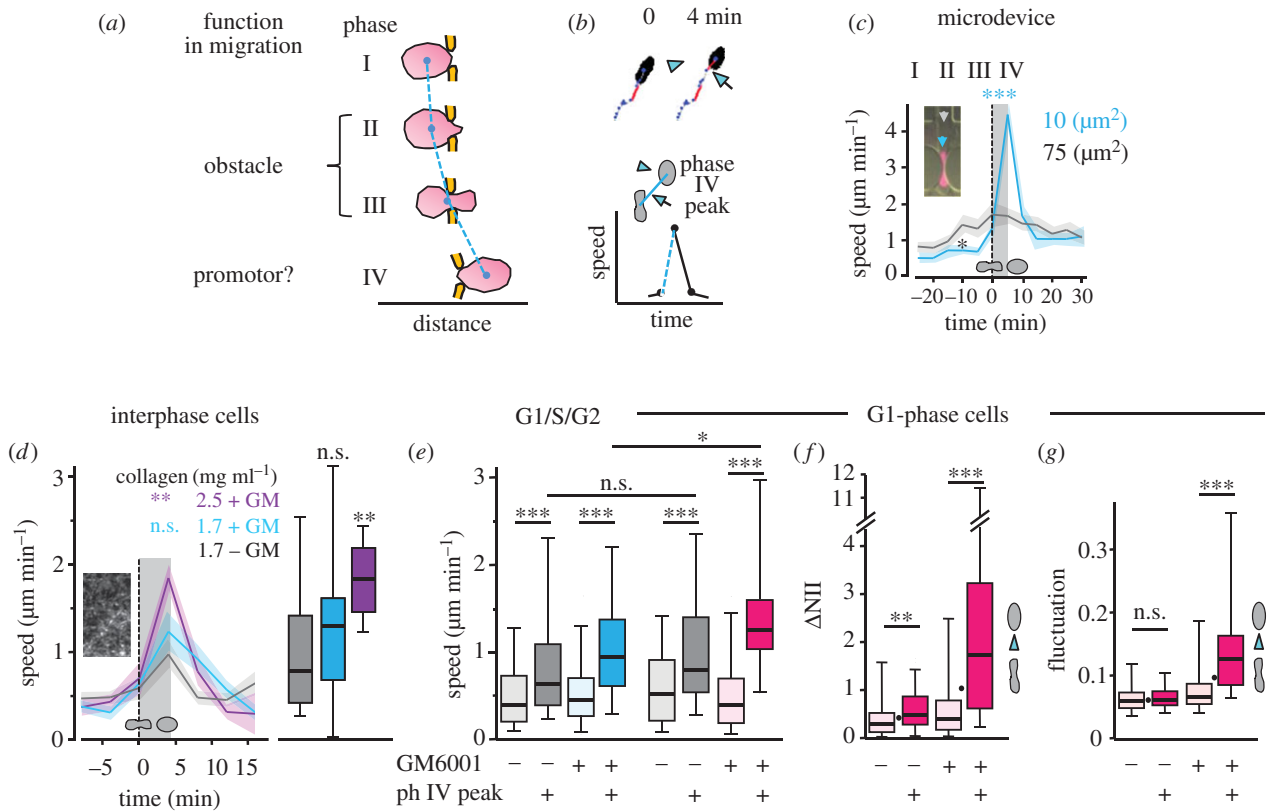
Figure 3. Characterization of 'phase IV' peak events. (a) Concept of nuclear deformation phases during cell migration through narrow pores. Adapted from Friedl *et al.* [13]. (b) Cartoon depicting selection scheme for phase IV speed peak values connected to nuclear rounding as shown in (c,d). (c) Speed of nuclei before (phase I and II), during (phase III) and after (phase IV) transmigration of pores of 75 μm^2 (grey) and 10 μm^2 (cyan) cross-section from microdevice. Vertical dotted line indicates time point when nuclei passed the centre of the pore (see inset), and grey shadowed area indicates phase IV. Solid lines represent mean, and shadowed coloured area $\pm$ s.e.m.; 16 and 18 cells per condition, $n = 3$. p-value was calculated for speed peaks at 5 min after pore passage of 10 μm^2 when compared with data from 75 μm^2 pores. Asterisk indicates decreased speed during passage of small when compared with large pores. (d) Quantification of phase IV speed peaks in collagen of decreasing effective pore size. The onset of each speed peak event was normalized to 0 min (dotted vertical line) and calculated based on speed increase in the moment of nuclear rounding (see black boxes in electronic supplementary material, figure S4,A-C, middle panels; S5A,B). $N = 1-3$; graphs are superimposed from 8 to 25 respective events from each 5 to 8 cells per condition monitored at high resolution; mean (coloured solid lines) $\pm$ s.e.m. (shadowed coloured areas). Grey shadowed area indicates phase IV event. Values of the peak speeds are also displayed as box plots. p-value was calculated for speed peaks at 4 min after pore passage, when compared with data from 1.7 mg ml^{-1} collagen in the absence of GM6001. (e–g) Depiction and analysis of either phase IV (strong colours) or all remaining non-phase IV events (light colours) from G1 cell-cycle phase cells (pink and grey), or mixed G1/S/G2 cell-cycle cells (blue and grey; e, left) after migration in collagen (1.7 mg ml^{-1}) and GM6001 where indicated. Analysis of (e) speed, (f) ΔNII as shown in figure 1i, and (g) nuclear fluctuation, as shown in figure 1j, with the difference that instead of a mean value per cell over time, values from each time point of a moving cell were defined and separated into phase IV peak and remaining events selected as in (b). The single dots in (f,g) depict the medians from the G1-phase cell results from figure 1i,j. (e, left; G1/S/G2 cells) $N = 1-3$; 50–79 phase IV peak events and 363–387 remaining events were analysed from nuclear sequences of 16–21 cells per condition. (e, right – g, G1 cells) $N = 1-3$; 24–53 phase IV peak events and 231–291 remaining events were analysed from nuclear sequences of 8–10 cells per condition. In (d–g), data are depicted as horizontal lines, boxes and whiskers for medians, 25th/75th and 5th/95th percentile. For all experiments, ***, $p \leq 0.001$; **, $p < 0.01$; ns, non-significant (both Mann–Whitney and Kolmogorov test).

corresponding nuclear shapes (NII) over time, normalized to the moment of nuclear rounding (phase IV peak) (figure 3b; electronic supplementary material, figure S5A,B; Movies S2, S5). This population analysis revealed, after a low-speed pore negotiation time, increased velocity peaks and, hence, speed oscillations for a population of single cells migrating through 10 μm^2 pores in engineered microdevices, whereas no peaks were generated in 75 μm^2 pores (figure 3c), consistent with data shown previously [37,39]. A similar stepwise peak acceleration, even though at lower velocity levels, was obtained with confinement in collagen (figure 3d). In G1 phase when compared with aggregated G1/S/G2 cells, speed peak events were again identified (electronic supplementary material, figure S5A,B). The individual

step-to-step speeds that G1/S/G2 cells performed during phase IV in confinement (blue box plot in figure 3e) were two times higher than the remaining migration steps, but were exceeded by around 25% in G1-phase nuclei (red box plot in figure 3e). Similarly, respective nuclear shape changes (ΔNII, fluctuation) during phase IV peaks were two- to five-fold higher in confinement when compared with remaining events and to phase IV peaks in cells migrating in collagen in the presence of proteolysis (figure 3f,g). This principle also held true when relating shape change and speed in confinement for a single cell-cycle progressing cell (electronic supplementary material, figure S2C,D and Movie S1). Together, despite overall deceleration of cell migration in strongly confining environments, phase IV peaks support

intermittent acceleration, and thereby sustained migration, in G1/S/G2 interphase cells. These accelerations are further increased in G1 cell-cycle cells only and, again, are associated with elastic deformation of G1-phase cell nuclei. By contrast, spatially optimized environments allow for effective speed throughout all phases of nuclear deformation, resulting in small or absent speed fluctuations.

(d) Experimental chromatin decondensation reduces shape change and impairs migration

To directly test whether chromatin condensation can promote phase IV peaks for sustained cell migration in confinement, we treated cells with chromatin decondensating TSA. Consistent with nuclear swelling after chromatin decondensation [20], and confirmed here by a relatively low cell number, nuclear size in G1-phase cells increased after TSA pre-treatment in a dose-dependent manner, but not yet at a concentration of $100 \, \text{ng ml}^{-1}$ (figure 4a). Accordingly, nuclear elasticity decreased in a dose-dependent manner (from 1 to 0.6 kPa; figure 4b) [34], confirming data from HeLa cells [26]. Besides softening of the nucleus, TSA pre-treatment decreased migration speed in confinement by 33–80% (figure 4c) and speed correlated positively with nuclear stiffness (figure 4d). Congruent to lowered elasticity after chromatin decondensation, nuclei deformed more slowly during migration and their ability to change shape reduced by up to 60% compared to an untreated control (figure 4e,f; electronic supplementary material, Movie S6). Accordingly, TSA treatment dampened phase IV accelerations (figure 4g), which for a TSA concentration of $100 \, \text{ng ml}^{-1}$ were not owing to an increase in nuclear size, but owing to a softened nucleus and a possibly less dynamic microtubule network, leading to overall decreased migration rates in confinement. Treatment with $500 \, \text{ng ml}^{-1}$ TSA entirely inhibited speed fluctuations, which might, in addition, be owing to the greatly increased nuclear size. Together, the data indicate that speed acceleration for effective migration in confinement requires chromatin condensation linked to high nuclear elasticity.

Besides chromatin condensation state, lamin A/C contributes to nuclear rigidity regulation. Downregulation of lamin A/C softens nuclei and supports migration rates through small pores [28,40,41]; however, its contribution to nuclear acceleration in phase IV remains unclear. Depletion of lamin A/C by RNAi reduced protein expression by 80% and nuclear stiffness by one third (our AFS analysis; data not shown), and was associated with a 40% decreased 'phase IV' speed acceleration when compared with untreated cells (figure 4h). These data are in agreement with an increased deformation of the softened cell nucleus of lamin A/C-deficient cells when compared with control cells during and after passage through small pores [37]. The somewhat higher migration rates during the remaining phases I–III (see asterisk) are indicative for the previously shown increased migration rate of cells after lamin A/C downregulation in confinement [29,40–42]. Together, the data indicate that the nuclear deformation energy during high confinement is released into nuclear rounding during phase IV peaking and is proportional to lamin A/C expression- and chromatin condensation-mediated nuclear elasticity.

3. Discussion

Here, we investigated 3D migration patterns of HT1080 fibrosarcoma cells in confining collagen lattices and microfabricated migration devices. The data reveal that cells and their nuclei do not migrate at a continuous speed, but undergo speed oscillations with velocities that increasingly deviate from beeline migration with confinement. Similar data of increasing nuclear oscillations in confinement presented by Yamada & colleagues [43] motivated a role of the cell nucleus in acting as a piston pressurizing the nucleo-anterior cell compartment and this way driving cell migration forward. Our findings complement these data well, stating that nuclear fluctuations were caused by increasing nuclear deformations with confinement. This led to migration delay during the pore negotiation process in phases I–III, and was followed by a short speed-up phase during the last transmigration phase IV. Similar to speed oscillations, nuclear shape changes become higher in amplitude with increasing confinement, and this could be attributed to the postulated increasing nuclear recoil phenomenon in phase IV after passage through a narrow pore [13]. Nuclear speed acceleration peaks were further responsive to nuclear elasticity regulation. Whereas with high stiffness and smaller size (i.e. during the G1 cell-cycle phase) speed oscillations were increased, conditions that soften the nucleus (e.g. in S/G2 cell-cycle phase, after experimental chromatin decondensation by TSA or by lamin A/C depletion) dampened periodic speed gain after pore passage.

Generally, processes connected with chromatin decondensation (e.g. mediated by cell cycle progression or by respective pharmacological inhibitors) reduce migration, in accordance with a number of publications. Yano and co-workers tested migration of Fucci-positive MKN45 adenocarcinoma cell spheroids in confining Gelfoam® gels, and observed the least effective outward migration for S/G2/M phase cells [44]. Likewise, by applying a novel nanoprinting technology to generate pores of defined areas on a smooth grated surface, S/G2 cell-cycle cells showed less pore engagement and penetration efficiency when compared with M/G1 and G1 cell-cycle phases [26]. Furthermore, chromatin decondensation agents TSA as well as MTA, a general protein methyltransferase inhibitor, step-wise reduced B16 melanoma migration in a transwell membrane assay of 8 and 5 µm diameter pores [20], in accordance to our results at comparable pore size ranges in collagen. Of note, stathmin-regulated microtubule dynamics by acetylation/deacetyation positively or negatively, respectively, regulates 3D cell migration [45]. Tubulin deacetylation by HDAC6 is inhibited by TSA [46], and thus delayed migration rates are likely not only owing to chromatin decondensation and softening, but also owing to stabilization of microtubules. In their transwell assay, Gerlitz and colleagues observed that the migration rate through 8 µm diameter pores was reduced by TSA to around 75%, but through confining 5 µm pore diameters to 60%, and by MTA to 70% (8 µm) and 30% (5 µm pores). These data support a dual effect of TSA, as well as by MTA, namely on the cell's general migratory machinery as well as on the impact of nuclear deformation by confinement, again affecting migration.

In summary, we investigated the phenomenon of pore transmigration by speed fluctuation and nuclear recoil in the context of tumour cell invasion. It will be interesting to test whether and how such oscillations during phases of
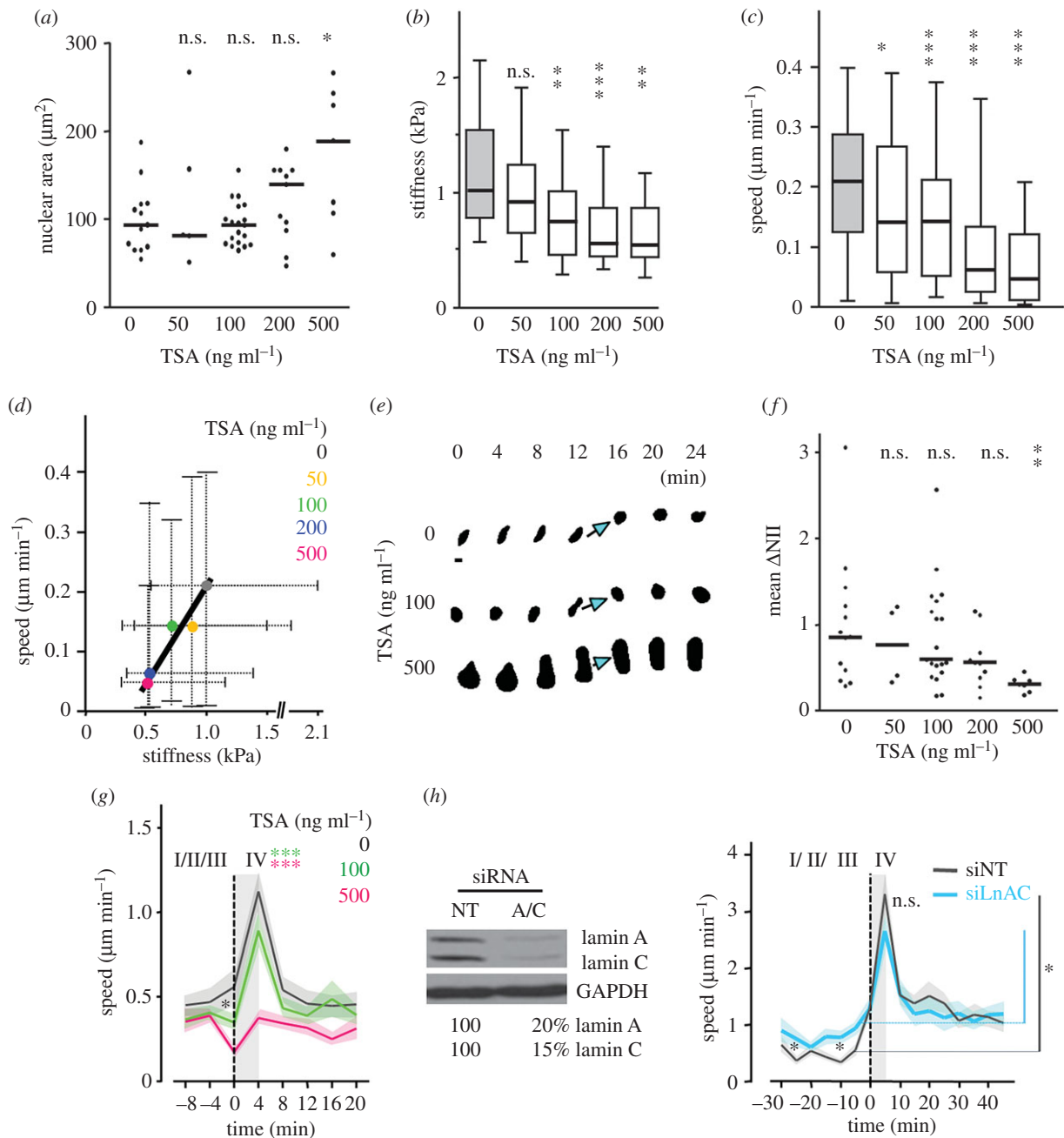
Figure 4. Altered stiffness, migration and reshaping of HT1080 cells and nuclei after TSA treatment or lamin A/C downregulation. Cells were pre-treated with indicated TSA concentrations or DMSO alone (indicated as 0 ng ml^{-1} TSA), and were either measured for elastic modulus (b) or migrated in collagen (1.7 mg ml^{-1}) in the presence of GM6001 (a,c–g). For all TSA experiments, except in (b) and (c), Fucci cells were used and G1-phase cells only were selected for analysis. (a) Nuclear areas after pre-treatment with TSA in collagen. Horizontal black lines show the medians. $N = 1$; 5–19 cells per TSA concentration. (b) Calculated stiffness at 1.5 nN contact force by bead-coupled cantilever probing using atomic force microscopy. $N = 1$–3; 14–37 cells per condition. (c) Mean cell migration efficacy per cell over 24 h with increasing concentrations of TSA. Cells that underwent mitosis during the recording were excluded from the analysis. $N = 3$; 66–90 cells per condition. (b,c) Horizontal black lines, boxes and whiskers show the medians, 25th/75th, and 10th and 90th (b) and 5th/95th (c) percentiles. (d) Correlation of stiffness with migration efficacy, using the medians and whiskers from (a,b). $R^2 = 0.92$. (e) Representative segmented nuclear sequences from migrating G1-phase (Fucci-red) cells at indicated time steps, in correspondence to Movie S6. Arrows indicate phase IV peak events based on speed increase and concomitant nucleus rounding. Bar, 10 μm. (f) Nuclear shape change during migration by TSA. Mean ΔNII per cell migrating over 0.3 to 10 h. Zero means no changes between subsequent nuclear shapes 5–19 cells per condition, shown as dots. Horizontal black lines show the medians. (g) Speed peaks, as in figure 3d, at indicated TSA concentrations. Graphs are superimposed from 22 to 38 respective events from each 7 to 19 cells per condition; $n = 1$. Mean (coloured solid lines) $\pm$ s.e.m. (shadowed coloured areas). Asterisk indicates decreased nuclear speed after TSA treatment before phase IV peak. (h) Left, lamin A/C expression intensity by western blot after transient downregulation by indicated siRNA (each 10 nM). Right, speed peaks in cells treated with non-targeting and lamin A/C siRNA after transmigration of 10 μm^2 pore in a microdevice. Asterisks indicate increased nuclear pore negotion speed after silamin A/C treatment before phase IV peak event. Each 21 cells per condition. (g,h right) Dotted vertical lines, speed peak at nuclear rounding; grey-shadowed areas, phase IV events. ***, $p \leq 0.001$; **, $p \leq 0.01$; *, $p \leq 0.05$; non-significant n.s. (a,b,c,f, Mann–Whitney test; g,h Students t-test).

active migration are interdependent on cell rear end detachment, and whether they occur also in other biological contexts, i.e. during development, immune responses, or tissue repair. Together, this knowledge will have an impact on the general understanding of cell migration mechanisms in heterogeneous environments.

4. Material and methods

(a) Fucci plasmid construction and lentivirus preparation

Plasmids pFucci-G1-Kusabira-Orange2 (Fucci-red) and pFucci-S-G2-M-Amazi Green1 (Fucci-green) [31] were purchased from MBL International. The IRES2 sequence was obtained by PCR using pIRES2-eGFP as template for primers 5′- GCG GAA TTC GTG TGT AGT ACT GTG TGT **GGA TCCGCC CCT CTC CCT C** -3′ and 5′-GCG CTC GAG GTG TGT CCC GGG GTG TGT **CCA TGG TTG TGG CCA TAT TAT C** -3′ (sequences in bold represent the IRES2 template-specific segments; underlined parts indicate restriction sites relevant for subsequent cloning steps). Obtained amplicon was digested with EcoRI and XhoI and inserted into pENTR-NotI/XhoI [47], creating pENTR-IRES2. An XmaI linker oligonucleotide (5′-TTA AGA CCC GGG TC-3′) was heated and allowed to cool to room temperature to obtain a heteroduplex oligonucleotide with AflII-compatible ends, which was subsequently introduced in the AflII site in pFucci-G1-Orange2. Consequently, the sequence encoding human Cdt1 coupled to monomeric Kusabira-Orange2 could be excised using XmaI and NcoI and transferred into XmaI/NcoI digested pENTR-IRES2, resulting in pENTR-IRES2-Orange2. Finally, the part encoding human Geminin coupled to monomeric Azami-Green1 was excised from pFucci-S-G2-M-Green by using EcoRI and HpaI, and inserted into EcoRI/ScaI digested pENTR-IRES2-Orange2. The resulting plasmid pENTR-Fucci was used as donor in a Gateway® LR recombination reaction with destination vector pLenti6.2/V5-DEST™ (Invitrogen), yielding pLenti-Fucci; a single bicistronic lentiviral vector that results in dual-colour fluorescent labelling of live cells that are either in G1 (here referred to as Fucci-red) or S/G2/M (here referred to as Fucci-green) cell-cycle phase. All constructs were sequence-verified.

(b) Cell lines, lentivirus production, cell culture and stable transduction of Fucci construct

The following cells were used: human HT1080 wild-type fibrosarcoma cells (ACC315; DSMZ Braunschweig; [4]); HT1080 dual-colour cells expressing cytoplasmic DsRed2 and nuclear histone-2B (H2B)−coupled EGFP [48]; HT1080 cells stably transfected with NLS-GFP [36] or H2B-mCherry; and HT1080 cells stably transfected with Fucci sensor. Cells were cultured in Dulbecco's modified Eagle medium (DMEM) supplemented with 10% fetal calf serum (FCS) containing L-glutamine (2 mM), sodium pyruvate (1 mM) and 100 U ml^{-1} penicillin, 100 µg ml^{-1} streptomycin and incubated at 37°C in a humidified 5% CO_2 atmosphere. Before cell experimentation, the detached and only loosely attached mitotic cells were washed away to only include interphase cells into all further assays.

For the generation of Fucci-positive HT1080 cells, recombinant lentiviral particles were produced, where in 10 cm dishes with 95% confluent HEK-293FT cell cultures were transfected overnight with JetPRIME reagent (Westburg) and a mixture of pLenti-Fucci plasmid and ViraPowerTM Packaging Mix (Invitrogen) according to the manufacturer's instructions. The following day, medium was refreshed and 48−72 h later virus-containing medium was harvested, passed through a 0.45 µm pore size filter and stored at −80°C until further use.

For stable transduction, HT1080 cells were seeded into six wells at 20−30% confluency, and on the next day medium was aspirated and 1 ml of viral-containing medium was drop-wise added to the cells and incubated overnight. On the following day, the medium was replaced with fresh medium, followed by selection with 5 µg ml^{-1} blasticidine for 4−5 days after the transduction. Blasticidine was constantly kept on the cells

during expansion, but removed 1−2 days prior to experimentation. Cells were sorted twice by flow cytometry for red or green fluorescence, resulting in a stable Fucci-positive cell population not higher, however, than around 70%. Dynamic imaging of 2D cultures revealed an approximated 90% rate of an appropriate cell-cycle-related temporal order of Fucci colours (data not shown). Cell growth characteristics of HT1080-Fucci-positive cells related to values measured for HT1080 cells previously, with cell cycle times of approximately 5 h in G1 phase, approximately 9 h in S/G2 phase and approximately 1.0 h in mitosis [34,49]. In addition, transfected cells remained functional with equal migration rates (0.2-0.4 µm min^{-1}) when compared with parental HT1080 cells [4]. These characteristics validate the applicability of the Fucci construct in HT1080 cells for investigating cell-cycle-related functions.

For transient lamin A/C knockdown, cells were cultured in antibiotics-free supplemented DMEM in six-well plates (each 250 000 cells) for 24 h. Cells were treated with a pool of small interfering (si) RNAs consisting of four single RNAs each and targeting expression of lamin A/C or non-targeting (NT) negative control (10 nM; on-target plus, SMARTpool; Dharmacon). The forward 21-nucleotide siRNA sequences for the NT control were 5-UGGUUUACAUGUCGACUAA-3, 5-UGGUUUACAUGUUGUGUGA-3, 5-UGGUUUACAUGUU UUCUGA-3, 5-UGGUUUACAUGUUUUCCUA-3; for si*LMNA* the forward sequences were 5-GAAGGAGGGUGACCUGAU A-3, 5-UCACAGCACGCACGCACUA-3, 5-UGAAAGCGCG CAAUACCAA-3, 5-CGUGUGCGCUCGCUGGAAA-3. siRNAs were transferred into cells with Dharmafect 4 transfection reagent according to the manufacturer's protocol and cultured with antibiotics-free DMEM for 48 h prior to characterization and functional studies. Lamin knockdown efficiency was determined by electrophoresis and western blot analysis from whole-cell lysates (62.5 mM Tris−HCl; 2% w/v SDS; 10% glycerol; 50 mM DTT; 0.01% w/v bromophenol blue), followed by chemiluminescence detection (ECL detection kit; GE Healthcare) and densitometric analysis (Fiji ImageJ).

(c) Analysis of the cell-cycle stage by flow cytometry

Flow cytometry was performed to determine the relative DNA amount in respect to Fucci colour within the cell population. Cultured HT1080 cells stably expressing Fucci marker were detached, re-suspended, and fixed with 500 µl 75% ice-cold ethanol for 1 h. Ethanol was carefully washed off and cells were incubated in 300 µl staining solution (1× PBS; 0.2 mg ml^{-1} RNase A, 1 µM DRAQ5) at 37°C for 30 min. Cells were measured on a CyAn ADP flow cytometer (Beckman Coulter) using spectral ranges 530/40 nm for Azami-Green1, 613/20 nm for Kusabira-Orange2 and 665/20 nm for DNA marker DRAQ5.

(d) Probing nuclear mechanics by atomic force spectroscopy

Two days before AFS experimentation, 40 000 cells were seeded into a Willco dish in 1 ml DMEM/10% FCS and incubated at 37°C in a humidified 5% CO_2 atmosphere. Twelve hours prior to the measurements, the medium was exchanged for 1 ml DMEM/10% FCS containing 10 mM HEPES (Gibco). Where indicated, cells were pre-treated with specified concentrations of histone deacetylase inhibitor trichostatin A (TSA, Sigma) 24 h before experimentation. Nuclear deformation measurements were performed using a Catalyst BioScope atomic force microscope (Bruker, Santa Barbara, CA, USA) combined with a three-channel confocal microscope TCS SP5 II (Leica, Mannheim, Germany) for simultaneous brightfield and epifluorescence imaging through a Hamamatsu (ORCA-05G) camera and an air objective (20×, 0.70 NA). Flexible NP-S cantilevers modified

with a 10 μm diameter bead were mounted, calibrated by the thermal noise method [50], and subsequently located over the cell for repeated probing (three to five times) at an approach and retraction rate of 10 μm s^{-1} each with a pre-defined force of 15 nN. The registered force–distance (F-D) curves were transferred into force-indentation (F-δ) curves and used to calculate the penetration, stiffness and dissipation of the nucleus [34]. The stiffness was calculated by using a custom algorithm written in IgorPro 6 (Wavemetrics) for fitting the F-δ curves with the Hertz model for spheres in contact with a flat surface [51]. The energy dissipated during compression of the cell/nucleus was derived by using a custom algorithm written in Matlab (MathWorks, Inc.) that determined the areas underneath the approach and retraction curves. Subsequently, the residual integral was calculated ($E_{dissipation} = E_{approach} - E_{retraction}$), which represents the energy needed to deform the nucleus; i.e. force (Newton) × distance (meter) = energy (Nm = J). The adhesion energy $E_{adhesion}$, measured as the area of the adhesion part in the retraction curve, was excluded because it is a measure of the stickiness of the bead probing the cell. Finally, to derive the relative dissipation energy during a probing cycle, $E_{dissipation}$ was divided by the energy needed to deform the nucleus ($E_{approach}$). The dissipation energy is an indicator for the viscous component of the visco-elastic properties of the cell. The elastic part of the cell is represented by its penetrability.

(e) Three-dimensional collagen assays, time-lapse microscopy and quantitative cell tracking

Three-dimensional collagen lattices were prepared from acidic collagen solution (rat tail, Corning; or bovine, Advanced Biomatrix) supplemented with Minimal Essential Eagle's Medium (MEM; Sigma), HEPES and NaOH (for rat tail collagen) or bicarbonate (for bovine collagen) reaching a pH ∼ 7.4, and mixed with the cell suspension to a final density of 200 000 cells ml^{-1} in collagen of indicated source and concentration. Usually, a concentration of 1.7 mg ml^{-1} rat tail collagen was used, unless indicated otherwise. Where indicated, cells were pre-treated with TSA for 24 h, and it was confirmed that cells remained viable, as judged by the absence of abnormal cell morphologies or blebbing, and as further quantified by a propidium iodide assay, as detailed in Krause *et al.* [34]. A 100 μl cell-collagen mix was added to each well of a 96-well glass-bottom plate, allowed to polymerize at 37°C in humidified 5% CO$_2$ atmosphere for 20–30 min, and was overlaid with medium. Where indicated, 5 μM GM6001 (Calbiochem) were added to both collagen and supernatant, and samples were monitored by temperature- and CO$_2$-controlled live microscopy over up to 24 h in 4 or 5 min frame intervals. Combined brightfield/fluorescence imaging was performed on either an Okobab microscope (10×, NA 0.25, Nikon DiaPhot 300, a Hamamatsu ORCA AG CCD camera, an excitation and emission filter set for FITC and TRITC, and the 2D time-lapse software Attovision), or on a spinning-disc confocal microscope (Pathway 855; BD Biosciences; 20x/0.40NA air objective; excitation filter sets of 488/10 and 548/20 nm, and emission filter sets of 520/35 nm and 600/15 nm). Life confocal microscopy for high-resolution imaging of HT1080 cells was performed in time-lapse z-stack mode using a temperature- and CO$_2$-controlled stage (37°C, 5%), and images were reconstructed as maximum intensity projections from all fluorescence and two reflection scans. Migration efficacy was quantified with the cell tracking program Autozell (v.1.0; Center for Computing and Communication Technologies (TZI), University of Bremen, Germany) of XY paths. The average speed per cell was calculated from the length of the migration path divided by time. Only viable cells that showed dynamic changes in cytoplasmic extensions and retractions were tracked and included into the analysis.

(f) Microfluidic migration devices

Polydimethylsiloxane (PDMS) microfluidic devices were fabricated and used as previously described [37,52], with a migration chamber height of 5 μm and a pore width of either 2 or 15 μm, resulting in 10 and 75 μm^2 cross-sectional areas. In brief, the migration devices were coated with 50 μg ml^{-1} rat tail type-I collagen (BD Biosciences) in acetic acid (0.02 N) overnight at 4°C and rinsed with imaging medium to remove the coating solution. After loading the cells, devices were incubated for at least 3 h to allow cell attachment before imaging. Microfluidic migration devices were imaged at 37°C on an inverted Zeiss Observer Z1 microscope equipped with a CCD camera (Photometrics CoolSNAP KINO) using a 20×/NA 0.8 air objective. The image acquisition was automated through ZEN (Zeiss) software with imaging intervals of 4 and 5 min collecting images for DIC and GFP. Time-series images were stabilized using a custom-written Matlab (Mathworks) script using features of the PDMS device as fiducials to compensate for the inaccuracy of the linear encoded microscope stage. Individual cells were tracked during the process of pore transmigration by using custom-developed Matlab software [53].

(g) Image analysis

For image analysis, in-focus nuclear areas and dynamic changes in nuclear shapes over time were analysed using the program Fiji ImageJ, or Matlab with the in-house built-in software ITNA (Image and Trajectory Nuclear Shape Analysis; Sussex University). Image stacks were separated into individual channels, thresholded (mostly by automated thresholding algorithm Otsu) and nuclear outlines per time point were automatically collected. From these outlines, nuclear area, nuclear irregularity index (NII), and nuclear fluctuation were calculated. NII analysis was conducted by computing shape properties using the Imaging Processing Toolbox provided by Matlab [54]. To calculate fluctuation, the two consecutive images were overlaid with their centroids and a 1°stepwise full-circle (360°) rotation was performed to find the maximum overlap between these two shapes (electronic supplementary material, Movie S3). The resulting fluctuation number was computed through

$$\text{Fluctuation} = \frac{A_1 + A_2 - 2(A_1 \cap A_2)}{A_1 + A_2},$$

where A_1, A_2 are the areas of the two consecutive nuclear shapes and $A_1 \cap A_2$ are the maximum intersections found through the rotation. The value range of this fluctuation number is (0,1). The value 0 indicates complete overlap of the nuclear shapes, while the value 1 implies no overlap at all. Phase IV events were defined as a combination of a NII value decrease (nuclear rounding) and a speed increase as a function of time, and selected after visual inspection, and were depicted as speed as a function of shape change (ΔNII).

(h) Statistics

Statistical analysis was performed on independent samples with non-Gaussian distribution, using both the two-tailed non-paired Mann–Whitney test and the two-sample Kolmogorov–Smirnov test. Independency of G1- and S/G2-phase samples was confirmed by the rejection of the null hypothesis (1% significance level; i.e. p-value = 0.01) and acceptance of the alternative hypothesis (99% confidence on the existence of a statistical significance between G1 and S/G2 phases).

References

1. Fidler IJ. 2003 The pathogenesis of cancer metastasis: the 'seed and soil' hypothesis revisited. *Nat. Rev. Cancer* **3**, 453–458. (doi:10.1038/nrc1098)

2. Paul CD, Mistriotis P, Konstantopoulos K. 2017 Cancer cell motility: lessons from migration in confined spaces. *Nat. Rev. Cancer* **17**, 131–140. (doi:10.1038/nrc.2016.123)

3. Weigelin B, Bakker GJ, Friedl P. 2012 Intravital third harmonic generation microscopy of collective melanoma cell invasion: principles of interface guidance and microvesicle dynamics. *IntraVital* **1**, 1–12. (doi:10.4161/intv.21223)

4. Wolf K et al. 2013 Physical limits of cell migration: control by ECM space and nuclear deformation and tuning by proteolysis and traction force. *J. Cell Biol.* **201**, 1069–1084. (doi:10.1083/jcb.201210152)

5. Lammerding J. 2011 Mechanics of the nucleus. *Compr. Physiol.* **1**, 783–807. (doi:10.1002/cphy.c100038)

6. Liu H, Wen J, Xiao Y, Liu J, Hopyan S, Radisic M, Simmons CA, Sun Y. 2014 In situ mechanical characterization of the cell nucleus by atomic force microscopy. *ACS Nano* **8**, 3821–3828. (doi:10.1021/nn500553z)

7. McGregor AL, Hsia CR, Lammerding J. 2016 Squish and squeeze—the nucleus as a physical barrier during migration in confined environments. *Curr. Opin. Cell Biol.* **40**, 32–40. (doi:10.1016/j.ceb.2016.01.011)

8. Fu Y, Chin LK, Bourouina T, Liu AQ, VanDongen AM. 2012 Nuclear deformation during breast cancer cell transmigration. *Lab Chip* **12**, 3774–3778. (doi:10.1039/c2lc40477j)

9. Thiam HR et al. 2016 Perinuclear Arp2/3-driven actin polymerization enables nuclear deformation to facilitate cell migration through complex environments. *Nat. Commun.* **7**, 10997. (doi:10.1038/ncomms10997)

10. Jayo A et al. 2016 Fascin regulates nuclear movement and deformation in migrating cells. *Dev. Cell* **38**, 371–383. (doi:10.1016/j.devcel.2016.07.021)

11. Wu J, Kent I, Shekhar N, Chancellor TJ, Mendonca A, Dickinson R, Lele T. 2014 Actomyosin pulls to advance the nucleus in a migrating tissue cell. *Biophys. J.* **106**, 7–15. (doi:10.1016/j.bpj.2013.11.4489)

12. Thomas DG et al. 2015 Non-muscle myosin IIB is critical for nuclear translocation during 3D invasion. *J. Cell Biol.* **210**, 583–594. (doi:10.1083/jcb.201502039)

13. Friedl P, Wolf K, Lammerding J. 2011 Nuclear mechanics during cell migration. *Curr. Opin. Cell Biol.* **23**, 55–64. (doi:10.1016/j.ceb.2010.10.015)

14. Fedorchak GR, Kaminski A, Lammerding J. 2014 Cellular mechanosensing: getting to the nucleus of it all. *Prog. Biophys. Mol. Biol.* **115**, 76–92. (doi:10.1016/j.pbiomolbio.2014.06.009)

15. Swift J et al. 2013 Nuclear lamin-A scales with tissue stiffness and enhances matrix-directed differentiation. *Science* **341**, 1240104. (doi:10.1126/science.1240104)

16. Kaufmann A, Heinemann F, Radmacher M, Stick R. 2011 Amphibian oocyte nuclei expressing lamin A with the progeria mutation E145 K exhibit an increased elastic modulus. *Nucleus* **2**, 310–319. (doi:10.4161/nucl.2.4.16119)

17. Schape J, Prausse S, Radmacher M, Stick R. 2009 Influence of lamin A on the mechanical properties of amphibian oocyte nuclei measured by atomic force microscopy. *Biophys. J.* **96**, 4319–4325. (doi:10.1016/j.bpj.2009.02.048)

18. Pajerowski JD, Dahl KN, Zhong FL, Sammak PJ, Discher DE. 2007 Physical plasticity of the nucleus in stem cell differentiation. *Proc. Natl Acad. Sci. USA* **104**, 15619–15624. (doi:10.1073/pnas.0702576104)

19. Stephens AD, Banigan EJ, Adam SA, Goldman RD, Marko JF. 2017 Chromatin and lamin A determine two different mechanical response regimes of the cell nucleus. *Mol. Biol. Cell* **28**, 1984–1996. (doi:10.1091/mbc.E16-09-0653)

20. Gerlitz G, Bustin M. 2010 Efficient cell migration requires global chromatin condensation. *J. Cell Sci.* **123**, 2207–2217. (doi:10.1242/jcs.058271)

21. Sarma K, Reinberg D. 2005 Histone variants meet their match. *Nat. Rev. Mol. Cell Biol.* **6**, 139–149. (doi:10.1038/nrm1567)

22. Hizume K, Araki S, Hata K, Prieto E, Kundu TK, Yoshikawa K, Takeyasu K. 2010 Nano-scale analyses of the chromatin decompaction induced by histone acetylation. *Arch. Histol. Cytol.* **73**, 149–163. (doi:10.1679/aohc.73.149)

23. Unnikrishnan A, Gafken PR, Tsukiyama T. 2010 Dynamic changes in histone acetylation regulate origins of DNA replication. *Nat. Struct. Mol. Biol.* **17**, 430–437. (doi:10.1038/nsmb.1780)

24. Bartova E, Krejci J, Harnicarova A, Galiova G, Kozubek S. 2008 Histone modifications and nuclear architecture: a review. *J. Histochem. Cytochem.* **56**, 711–721. (doi:10.1369/jhc.2008.951251)

25. Toth KF et al. 2004 Trichostatin A-induced histone acetylation causes decondensation of interphase chromatin. *J. Cell Sci.* **117**, 4277–4287. (doi:10.1242/jcs.01293)

26. Panagiotakopoulou M, Bergert M, Taubenberger A, Guck J, Poulikakos D, Ferrari A. 2016 A nanoprinted model of interstitial cancer migration reveals a link between cell deformability and proliferation. *ACS Nano* **10**, 6437–6448. (doi:10.1021/acsnano.5b07406)

27. Chalut KJ et al. 2012 Chromatin decondensation and nuclear softening accompany Nanog downregulation in embryonic stem cells. *Biophys. J.* **103**, 2060–2070. (doi:10.1016/j.bpj.2012.10.015)

28. Harada T et al. 2014 Nuclear lamin stiffness is a barrier to 3D migration, but softness can limit survival. *J. Cell Biol.* **204**, 669–682. (doi:10.1083/jcb.201308029)

29. Davidson PM, Denais C, Bakshi MC, Lammerding J. 2014 Nuclear deformability constitutes a rate-limiting step during cell migration in 3-D environments. *Cell. Mol. Bioeng.* **7**, 293–306. (doi:10.1007/s12195-014-0342-y)

30. Greiner AM, Scheiwe AC, Stamow DR, Autenrieth TJ, Lahann J, Franz CM, Bastmeyer M. 2014 Multifunctional polymer scaffolds with adjustable

pore size and chemoattractant gradients for studying cell matrix invasion. *Biomaterials* **35**, 611 – 619. (doi:10.1016/j.biomaterials.2013.09.095)

31. Sakaue-Sawano A *et al.* 2008 Visualizing spatiotemporal dynamics of multicellular cell-cycle progression. *Cell* **132**, 487 – 498. (doi:10.1016/j.cell.2007.12.033)

32. Filippi-Chiela EC, Oliveira MM, Jurkovski B, Callegari-Jacques SM, Silva VD, Lenz G. 2012 Nuclear morphometric analysis (NMA): screening of senescence, apoptosis and nuclear irregularities. *PLoS ONE* **7**, e42522. (doi:10.1371/journal.pone.0042522)

33. Marcus JM, Burke RT, DeSisto JA, Landesman Y, Orth JD. 2015 Longitudinal tracking of single live cancer cells to understand cell cycle effects of the nuclear export inhibitor, selinexor. *Sci. Rep.* **5**, 14391. (doi:10.1038/srep14391)

34. Krause M, Te Riet J, Wolf K. 2013 Probing the compressibility of tumor cell nuclei by combined atomic force-confocal microscopy. *Phys. Biol.* **10**, 065002. (doi:10.1088/1478-3975/10/6/065002)

35. Wolf K, Wu YI, Liu Y, Geiger J, Tam E, Overall C, Stack MS, Friedl P. 2007 Multi-step pericellular proteolysis controls the transition from individual to collective cancer cell invasion. *Nat. Cell Biol.* **9**, 893 – 904. (doi:10.1038/ncb1616)

36. Denais CM *et al.* 2016 Nuclear envelope rupture and repair during cancer cell migration. *Science* **352**, 353 – 358. (doi:10.1126/science.aad7297)

37. Davidson PM, Sliz J, Isermann P, Denais C, Lammerding J. 2015 Design of a microfluidic device to quantify dynamic intra-nuclear deformation during cell migration through confining environments. *Integr. Biol.* **7**, 1534 – 1546. (doi:10.1039/c5ib00200a)

38. Gerlitz G, Bustin M. 2011 The role of chromatin structure in cell migration. *Trends Cell Biol.* **21**, 6 – 11. (doi:10.1016/j.tcb.2010.09.002)

39. Lautscham LA *et al.* 2015 Migration in confined 3D environments is determined by a combination of

adhesiveness, nuclear volume, contractility, and cell stiffness. *Biophys. J.* **109**, 900 – 913. (doi:10.1016/j.bpj.2015.07.025)

40. Yadav SK, Feigelson SW, Roncato F, Antman-Passig M, Shefi O, Lammerding J, Alon R. 2018 Elevated nuclear lamin A is permissive for granulocyte transendothelial migration but not for motility through collagen I barriers. *J. Leukoc. Biol.* **104**, 239 – 251. (doi:10.1002/JLB.3HI1217-488R)

41. Rowat AC *et al.* 2013 Nuclear envelope composition determines the ability of neutrophil-type cells to passage through micron-scale constrictions. *J. Biol. Chem.* **288**, 8610 – 8618. (doi:10.1074/jbc.M112.441535)

42. Infante E *et al.* 2018 LINC complex-Lis1 interplay controls MT1-MMP matrix digest-on-demand response for confined tumor cell migration. *Nat. Commun.* **9**, 2443. (doi:10.1038/s41467-018-04865-7)

43. Petrie RJ, Harlin HM, Korsak LI, Yamada KM. 2017 Activating the nuclear piston mechanism of 3D migration in tumor cells. *J. Cell Biol.* **216**, 93 – 100. (doi:10.1083/jcb.201605097)

44. Yano S *et al.* 2014 Invading cancer cells are predominantly in G0/G1 resulting in chemoresistance demonstrated by real-time FUCCI imaging. *Cell Cycle* **13**, 953 – 960. (doi:10.4161/cc.27818)

45. Belletti B *et al.* 2008 Stathmin activity influences sarcoma cell shape, motility, and metastatic potential. *Mol. Biol. Cell* **19**, 2003 – 2013. (doi:10.1091/mbc.E07-09-0894)

46. Zilberman Y, Ballestrem C, Carramusa L, Mazitschek R, Khochbin S, Bershadsky A. 2009 Regulation of microtubule dynamics by inhibition of the tubulin deacetylase HDAC6. *J. Cell Sci.* **122**, 3531 – 3541. (doi:10.1242/jcs.046813)

47. Bourgonje AM *et al.* 2014 Intracellular and extracellular domains of protein tyrosine phosphatase PTPRZ-B differentially regulate glioma cell growth and motility. *Oncotarget* **5**, 8690 – 8702. (doi:10.18632/oncotarget.2366)

48. Yamamoto N *et al.* 2004 Cellular dynamics visualized in live cells in vitro and in vivo by differential dual-color nuclear-cytoplasmic fluorescent-protein expression. *Cancer Res.* **64**, 4251 – 4256. (doi:10.1158/0008-5472.CAN-04-0643)

49. Sayers CM, Papandreou I, Guttmann DM, Maas NL, Diehl JA, Witze ES, Koong AC, Koumenis C. 2013 Identification and characterization of a potent activator of p53-independent cellular senescence via a small-molecule screen for modifiers of the integrated stress response. *Mol. Pharmacol.* **83**, 594 – 604. (doi:10.1124/mol.112.081810)

50. te Riet J *et al.* 2011 Interlaboratory round robin on cantilever calibration for AFM force spectroscopy. *Ultramicroscopy* **111**, 1659 – 1669. (doi:10.1016/j.ultramic.2011.09.012)

51. Digman MA, Brown CM, Horwitz AR, Mantulin WW, Gratton E. 2008 Paxillin dynamics measured during adhesion assembly and disassembly by correlation spectroscopy. *Biophys. J.* **94**, 2819 – 2831. (doi:10.1529/biophysj.107.104984)

52. Keys J, Windsor A, Lammerding J. 2018 Assembly and use of a microfluidic device to study cell migration in confined environments. In *The LINC complex. methods in molecular biology*, vol. 1840 (eds G Gundersen, H Worman), pp. 101 – 118. New York, NY: Humana Press.

53. Elacqua JJ, McGregor AL, Lammerding J. 2018 Automated analysis of cell migration and nuclear envelope rupture in confined environments. *PLoS ONE* **13**, e0195664. (doi:10.1371/journal.pone.0195664)

54. Gonzalez RC, Woods RE, Eddins SL. 2009 *Digital image processing using MATLAB*, 2nd edn. USA: Gatesmark Publishing.

55. Krause M *et al.* 2019 Data from: Cell migration through three-dimensional confining pores: speed accelerations by deformation and recoil of the nucleus. Dryad Digital Repository. (doi:10.5061/dryad.c806hk2)